Transmission properties and physical mechanisms of X-ray communication for blackout mitigation during spacecraft reentry

Yunpeng Liu,[1,2,a)] Huan Li,[1,a)] Yanlong Li,[1] Shuang Hang,[1] and Xiaobin Tang[1,2,b)]
[1]*Department of Nuclear Science and Engineering, Nanjing University of Aeronautics and Astronautics, Nanjing 211106, China*
[2]*MIIT Key Laboratory of Material Preparation and Protection Technology for Harsh Environment, Nanjing 211106, China*

(Received 3 August 2017; accepted 25 October 2017; published online 8 November 2017)

Recent advances in X-ray science have witnessed the X-ray communication (XCOM), a new revolutionary technology first proposed by NASA since 2007. In combination with the advanced modulated X-ray source, XCOM shows a promising prospect for helping to alleviate the occurrence of inevitable blackout communication by using the regular radio frequency (RF) signal, paving the way towards realizing real-time communication during spacecraft reentry into atmosphere. Here, we acquired the detailed information of electron density distribution of plasma sheath encountered during vehicle reentry through Computational Fluid Dynamics simulation. Based on these derived parameters, Finite-difference Time-domain method was employed to investigate the transmission properties of X-rays through the plasma sheath, and the results indicated that X-ray transmission was not influenced by the reentry plasma sheath at different reentry altitudes and spacecraft surface positions compared with RF signal. In addition, 2D Particle-In-Cell simulation was also adopted to provide deeper insight into the transmission properties and physical mechanisms of X-ray carrier propagating through the plasma sheath, and results showed that the transmission coefficient was over 0.994 and the observation of plasma channel effect was also an important signature, which was of great importance to X-ray propagating through the plasma sheath. *Published by AIP Publishing.* https://doi.org/10.1063/1.4998786

I. INTRODUCTION

Blackout communication occurs at the altitudes ranging from 20 km to 100 km up to several minutes when a supersonic spacecraft reenters the Earth's atmosphere, owing to the tremendous heat generated by air compression and ablation surrounding the vehicle, known as plasma sheath.[1,2] The ionized surrounding fluids interfere with the regular radio frequency (RF) signal, leading to the severe attenuation of the communication signal between the reentry vehicles and the ground stations. Thus far, considerable research efforts have been devoted to mitigating blackout communication, including the use of aerodynamic shapes,[3] injection of electrophilic materials,[4] static electromagnetic field,[5] and transmission at higher frequencies.[6] However, none of these off-the-shelf schemes is satisfactory because of their shortcomings in practice and insurmountable engineering obstacles.[7]

Fortunately, X-ray communication (XCOM), a revolutionary concept first proposed by Dr. Keith Gendreau of NASA in 2007,[8] exploits X-ray with extremely low beam divergence as a communication carrier to realize high-rate, deep-space, low transmit power, highly physically secure data links,[9] which opens a new route to enable communications through harsh hypersonic plasma environments. Similar to those of microwave, optical, laser, and RF communications, X-ray is also a form of electromagnetic wave which could be used as a communication carrier to transfer information by digital modulation schemes such as a constant amplitude and phase or frequency. X-rays possess a wavelength ranging from 0.01 nm to 10 nm, corresponding to frequencies in the range[10] 3.0×10^{16} Hz to 3.0×10^{19} Hz which could meet future enormous data center bandwidth demands. Proof-of-principle experiments have shown the feasibility of XCOM. For example, NASA had demonstrated the world's first XCOM system using a modulated X-ray source, with the hope of increasing the system's data rate of 50 kbps to 1 Mbps.[8] Kealhofer *et al.* discovered ultrafast laser-triggered X-ray emission from hafnium carbide tips for space-based communications.[11] Porter found that the data rate of each X-ray link with 3.0×10^{19} Hz range could reach 40 Petabits/s through on-off keying (OOK) modulation.[12] In our previous work, we have certified the feasibility of XCOM through a plasma sheath encountered during spacecraft reentry.[13] However, the transmission properties and physical mechanisms of XCOM during the reentry plasma sheath have not been referred in previous works or even in the existing literature. Therefore, further efforts are still required to understand and explore more details on the theoretical analysis of the X-ray carrier interaction with the plasma sheath in order to surmount blackout communication better.

In this work, the Computational Fluid Dynamics (CFD) method was utilized to obtain more detailed electron density distributions of the plasma sheath around reentry vehicles, followed by the investigation on X-ray interaction with the

[a)]Y. Liu and H. Li contributed equally to this work.
[b)]Author to whom correspondence should be addressed: tangxiaobin@nuaa.edu.cn. Tel.: +86 13601582233. Fax: +86 025 52112908-80407.

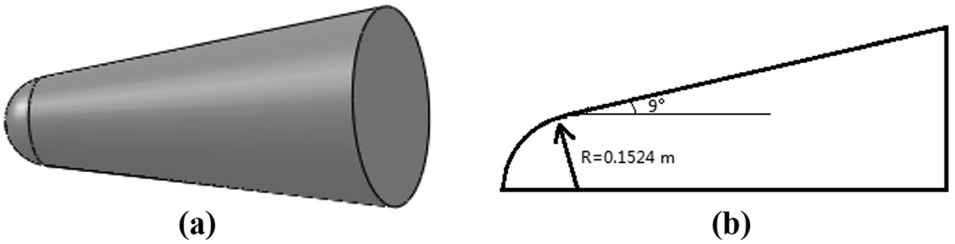

FIG. 1. (a) Three and (b) two dimensional model of RAM C-II spacecraft used in this simulation.

plasma sheath through the Finite Difference Time Domain (FDTD) algorithm to analyze the transmission properties of X-ray. Additionally, we first studied the physical mechanism of X-ray communication carrier through a plasma sheath by employing 2D Particle-In-Cell (PIC) simulation, and the transmission properties were taken into account as well.

II. THEORIES AND METHODS

A. Computational fluid dynamics (CFD) method

The Radio Attenuation Measurement (RAM) experiment has conducted a series of hypersonic flights in the 1960s to investigate blackout communication.[14,15] The 3D geometry of the RAM C-II spacecraft, a blunt cone, is shown in Fig. 1(a), which is used to evaluate the modeling of weakly ionized gases. The nose radius $R = 0.1524\,m$, the half cone angle $\alpha_c = 9°$, and the whole length $L = 1.295\,m$.[15] For simplicity, the geometry was converted into the 2D model in Fig. 1(b) due to its axial symmetry. In this section, we expect to investigate the detailed electron distribution profiles of plasma sheath formed around the vehicle surface to clarify the reason why blackout communication occurs, and then analyze the potential application of X-ray communication through a plasma sheath based on these obtained data, which are seldom focused in the existing studies.

The ANSYS FLUENT code[16] based on CFD numerical algorithm with the theromodynamic and transport property evaluation was employed to calculate the aerodynamics coefficients of the compressed layer near the surface of the spacecraft and obtain the electron density distribution (N_e) profile of the plasma sheath during reentry at hypersonic speeds. It is worth mentioning that multi-physical field coupling should be applied due to the model of non-equilibrium physical and chemical reactions in the plasma sheath during spacecraft speed of more than 7 km/s at altitudes ranging from 20 km to 90 km. The flow was modelled as a reacting gas (air) in thermochemical nonequilibrium and chemical nonequilibrium described by the viscous Navier-Stokes equations, and it was assumed to be laminar and continuum.

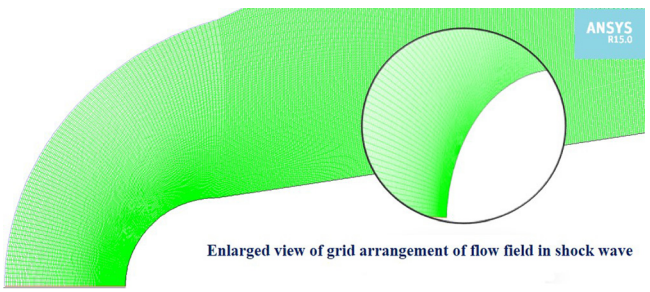

FIG. 2. Computational grid system of blunt RAM C-II spacecraft flow field, and the inset amplified circle diagrams denote the enlarged view of grid arrangement of flow field in the shock wave.

Gambit software was used for grid-generation across the total fluid region, in which the grid points of vehicle surface should be more refined because there exist shock waves generated around it. Therefore, the physical space was discretized into non-uniform grid points as shown in Fig. 2. In the simulation, considering the effect of the computational domain, the stretching factor to control the grid points intensity near the surface, and the grids points number in the axial and normal directions, grid independence tests were performed. The finer mesh discretization of vehicle surface contributes to obtain more precise flow field, and the coarse grid points far away from the stagnation region of the vehicle help in reducing the computational time.

The wall boundary condition was presumed to be noncatalytic, which meant that the normal gradient of each species mass fraction is 0 at the wall. The inflow parameters of the boundaries conditions such as the freestream velocity, density, and temperature were set with altitudes at 25, 31, and 62 km according to the flight environments listed in Table I,[17] and the surface temperature was presumed constant at 1500 K. The transport properties were evaluated through Wilke's mixing rule[18] and Blottner model,[19] and the diffusion coefficient was obtained using a constant Lewis number. All of the approximations were still adequate for a 7 km/s hypersonic flow field.

Also, for ionized air region behind the shock wave front at speeds of $v < 9\,km/s$, the Dunnn-Kang model consisting of seven species (N_2, O_2, NO, N, O, NO^+, and e^-) and the primary 20 chemical reactions were considered in our simulation.[20,21] These reactions involve the dissociation-recombination, exchange reactions, associative-ionization and its inverse the dissociative-recombination reaction. Wilson[22] indicated that the electron-impact ionization dominated for shock speeds below 9 km/s. In addition, Takahashi[23] discovered that the electrons generated around the spacecraft behind the shock wave are mainly due to the associative-ionization contribution, and the effect of electron-impact ionization reactions to electron generation is relatively small because of the lower temperature in the shock layer. At high temperatures, the

TABLE I. Initial freestream conditions for the numerical CFD modeling.[17]

Altitude (km)	Density (kg/m^3)	Temperature (K)	Velocity (m/s)
62	2.73×10^{-4}	247.0	7650
31	1.84×10^{-2}	226.5	6550
25	4.01×10^{-2}	221.5	5120

TABLE II. Finite rate chemistry model used in the simulation. [k_{fi}/k_{bi} ($m^3\ mol^{-1}\ s^{-1}$)].[24]

Number	Reactions	A_{fi}	B_{fi}	C_{fi}	A_{bi}	B_{bi}	C_{bi}
1	$O_2+O_2 \rightleftharpoons 2O+O_2$	3.24×10^{13}	−1	5.95×10^{4}	2.70×10^{4}	−0.5	0
2	$O_2+N_2 \rightleftharpoons 2O+N_2$	7.20×10^{12}	−1	5.95×10^{4}	6.00×10^{3}	−0.5	0
3	$O_2+NO \rightleftharpoons 2O+NO$	3.60×10^{12}	−1	5.95×10^{4}	3.00×10^{3}	−0.5	0
4	$O_2+O \rightleftharpoons 3O$	9.00×10^{13}	−1	5.95×10^{4}	7.50×10^{4}	−0.5	0
5	$O_2+N \rightleftharpoons 2O+N$	3.60×10^{12}	−1	5.95×10^{4}	3.00×10^{3}	−0.5	0
6	$O_2+N_2 \rightleftharpoons 2N+O_2$	1.90×10^{11}	−0.5	1.13×10^{5}	1.10×10^{4}	−0.5	0
7	$2N_2 \rightleftharpoons 2N+N_2$	4.70×10^{11}	−0.5	1.13×10^{5}	2.72×10^{4}	−0.5	0
8	$N_2+NO \rightleftharpoons 2N+NO$	1.90×10^{11}	−0.5	1.13×10^{5}	1.10×10^{4}	−0.5	0
9	$N_2+O \rightleftharpoons 2N+O$	1.90×10^{11}	−0.5	1.13×10^{5}	1.10×10^{4}	−0.5	0
10	$N_2+N \rightleftharpoons 3N$	4.09×10^{16}	−1.5	1.13×10^{5}	2.72×10^{9}	−1.5	0
11	$O_2+NO \rightleftharpoons O+N+O_2$	3.90×10^{14}	1.5	7.55×10^{4}	1.00×10^{8}	−1.5	0
12	$N_2+NO \rightleftharpoons O+N+N_2$	3.90×10^{14}	1.5	7.55×10^{4}	1.00×10^{8}	−1.5	0
13	$2NO \rightleftharpoons O+N+NO$	7.80×10^{14}	−1.5	7.55×10^{4}	2.00×10^{8}	−1.5	0
14	$O+NO \rightleftharpoons 2O+N$	7.80×10^{14}	−1.5	7.55×10^{4}	2.00×10^{8}	−1.5	0
15	$N+NO \rightleftharpoons O+2N$	7.80×10^{14}	−1.5	7.55×10^{4}	2.00×10^{8}	−1.5	0
16	$O_2+N_2 \rightleftharpoons 2NO+e^-$	1.38×10^{14}	−1.84	1.41×10^{5}	1.00×10^{12}	−2.5	0
17	$N_2+NO \rightleftharpoons N_2+NO^++e^-$	2.20×10^{9}	−0.35	1.08×10^{5}	2.20×10^{14}	−2.5	0
18	$O_2+NO \rightleftharpoons O_2+NO^++e^-$	8.80×10^{9}	−0.35	1.08×10^{5}	8.80×10^{14}	−2.5	0
19	$N+O \rightleftharpoons NO^++e^-$	1.40	1.5	3.19×10^{4}	6.70×10^{15}	−1.5	0
20	$N_2+O \rightleftharpoons NO+N$	7.00×10^{7}	0	3.80×10^{4}	1.56×10^{7}	0	0

reaction of collisional ionization and ion-molecule reactions should be considered. That is, eleven species chemicals model would be more accurate. However, these mechanisms are not considered in the present study, especially in the lower temperature regime. The forward k_{fi} and backward k_{bi} rate constants for reaction were modelled employing the Arrhenius expression[24]

$$k_{fi} = A_{fi}T^{B_{fi}}\exp\left(-\frac{C_{fi}}{T}\right), \tag{1}$$

$$k_{bi} = A_{bi}T^{B_{bi}}\exp\left(-\frac{C_{bi}}{T}\right), \tag{2}$$

where i indicates the number of chemical reactions, and the reaction coefficient values of various constants of the model are shown in Table II.

B. Finite-difference time-domain (FDTD) method

In fact, the reentry plasma sheath is non-uniformly distributed and can be characterized by two important parameters, namely, electron density (N_e) and collision frequency (v_c). In this section, the theoretical Finite-difference time-domain (FDTD) method was used to analyze X-ray interaction with plasma sheath and investigate X-ray transmission properties through these plasma density profiles obtained from the CFD results, which was different from the Wentzel–Kramers–Brillouin (WKB) approximation method in our previous study.[13] Considering an isotropic non-magnetized cold plasma, the kinetic Maxwell's equations and constitutive relation can be given by[25]

$$\nabla\times\boldsymbol{E} = -\mu_0\frac{\partial\boldsymbol{H}}{\partial t}, \tag{3}$$

$$\nabla\times\boldsymbol{H} = \varepsilon_0\frac{\partial\boldsymbol{E}}{\partial t}+\boldsymbol{J}, \tag{4}$$

$$\frac{d\boldsymbol{J}}{dt}+v_c\boldsymbol{J} = \varepsilon_0 w_p^2\boldsymbol{E}, \tag{5}$$

where μ_0 and ε_0 are the permeability and permittivity of free space, $\boldsymbol{E}$ is the electric field, $\boldsymbol{H}$ denotes the magnetic intensity, J is the polarization current density, and w_p means plasma frequency and can be expressed as[25]

$$w_p = \sqrt{\frac{N_e e^2}{\varepsilon_0 m_e}}, \tag{6}$$

where N_e represents plasma density distribution, m_e is the electron mass, and e is the electron charge.

From LTJEC-FDTD algorithm,[26] we can update the discrete forms of (7)–(9) as follows:

$$E_x^{n+1}(k) = E_x^n(k)-\frac{\Delta t}{\varepsilon_0\Delta z}\left[H_y^{n+0.5}(k+0.5)-H_y^{n+0.5}(k-0.5)\right] -\frac{\Delta t}{\varepsilon_0}J_x^{n+0.5}(k), \tag{7}$$

$$H_y^{n+0.5}(k+0.5) = H_y^{n-0.5}(k+0.5) -\frac{\Delta t}{\mu_0\Delta z}\left[E_x^n(k+1)-E_x^n(k)\right], \tag{8}$$

$$J_x^{n+0.5}(k) = e^{-v_c\Delta t}J_x^{n-1}(k)+\varepsilon_0\omega_p^2\Delta t\cdot e^{-\frac{v_c\Delta t}{2}}E_x^n(k). \tag{9}$$

The FDTD spatial discretization was set to be $\Delta z = 7.5\times10^{-5}$ for the RF carrier and $\Delta z = 1.3\times10^{-10}$ for X-ray carrier, respectively. The temporal step was $\Delta t = \Delta z/(2c) = 0.125$ ps. The attenuation coefficient (Att) and

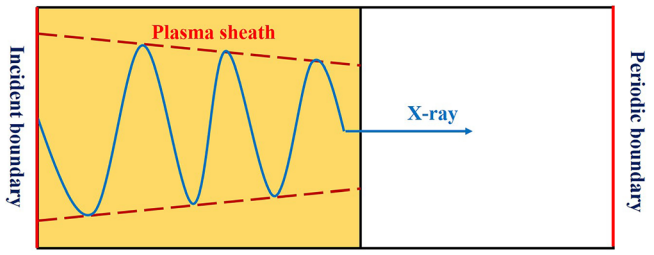

FIG. 3. Schematic of X-ray laser pulse propagated in an underdense fully ionized plasma sheath.

transmission coefficient (T) were calculated to evaluate the transmission properties of X-rays (10^{17} –10^{18} Hz analyzed) in the plasma sheath obtained from CFD results, and then explain the advantage of XCOM in radio blackout compared with RF signals. In addition, the relevant results of RF carrier were used for comparison with X-ray, and the related behavior of electromagnetic waves' propagation for RF carrier was investigated in Takahashi's work by calculating the signal loss using the FD2TD method.[22,27] To some extent, these two parameters could reflect the transmission properties of X-rays in the plasma sheath.

C. Particle-in-cell (PIC) simulation

The two-dimensional (2 D) EPOCH PIC simulation[28] was considered to study the transmission properties and physical mechanisms of X-ray carrier signal interaction with plasma sheath. When the modulated X-ray laser pulse length cτ (where c is the light speed and τ is the pulse duration) is comparable to the plasma wavelength λ_p, the X-ray laser wakefield acceleration comes into effect, which leads to a series of nonlinear physical phenomena.[29,30]

As shown in Fig. 3, the simulation was carried out with a box that was $X \times Y = 300\lambda_0 \times 200\lambda_0$, sampled by 300 × 200 cells with 10 macro-particles in the longitudinal and transverse directions, respectively, where $\lambda_0 = 10$ nm represented the X-ray laser wavelength. In this simulation, a linearly modulated X-ray laser pulse propagated in an underdense nitrogen and helium plasma, and the electron density distribution of plasma sheath was set according to the previous CFD simulation results. The X-ray laser pulse was launched from the left side of the box at $t = 0$, and the wakefield was driven in plasma sheath by X-ray laser pulse with transverse Gaussian envelope with the pulse peak normalized amplitude of $a_0 = 4$. The X-ray laser pulse duration was 30 fs, and the initial spot size was 2 μm FWHM (radius at $1/e^2$ of maximum intensity).

III. RESULTS AND DISCUSSION

A. Electron density distributions of plasma sheath

Predicting the electron density distribution profile of the plasma sheath around the supersonic vehicle is of great importance for elucidating the origin of blackout communication during atmosphere reentry. In this section, we employed CFD technique to exploit the electron distributions of the plasma at various altitudes of 62, 31, and 25 km. As illustrated in Fig. 4, a region appears to exist in which the electron density distribution generated by the shock layer remains relatively high at each altitude. The distribution range of the electron density profile around the vehicle varies from 10^9 cm^{-3} to 10^{14} cm^{-3}, which is consistent with the

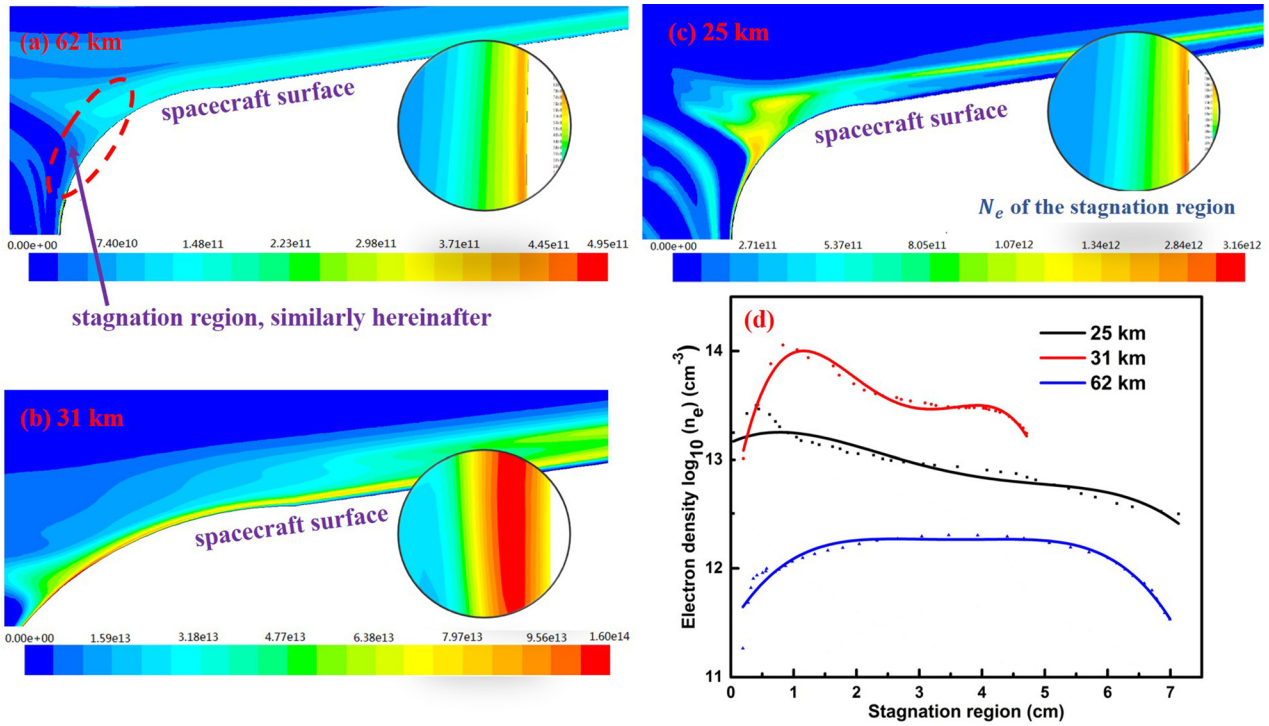

FIG. 4. Electron density distributions of plasma sheath around the vehicle surface encountered during reentry into atmosphere at an altitude of (a) 62 km, (b) 31 km, and (c) 25 km. The inset amplified circle diagrams denote the electron density distribution of the stagnation region. (d) The electron density peak distributions along the stagnation region at three reentry altitudes, for comparison.

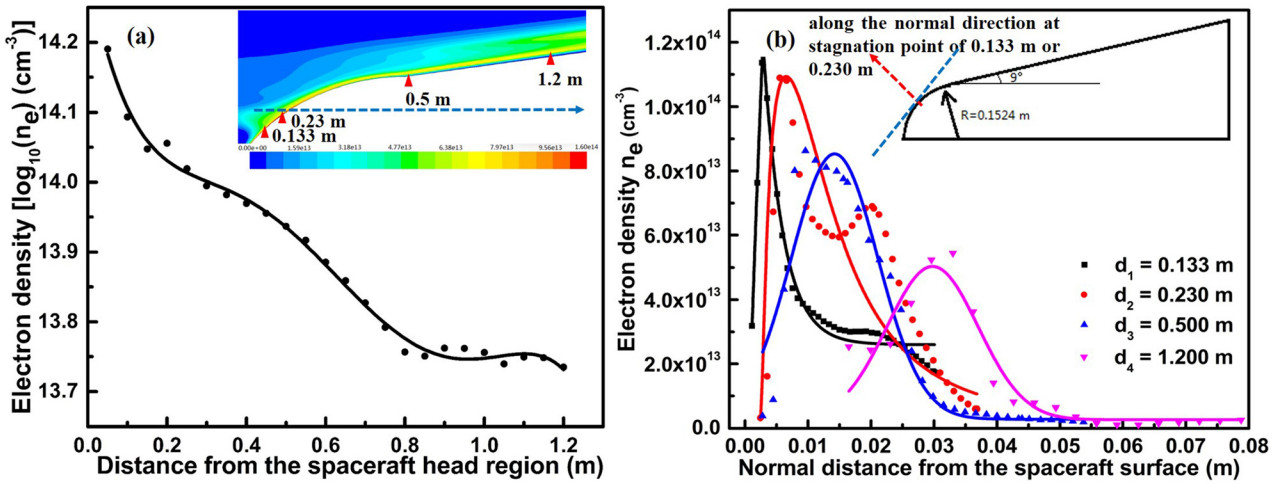

FIG. 5. (a) Variation of the electron density peak distribution around the vehicle with different distances from the spacecraft head region at the altitude of 31 km. (b) The normal direction of electron density distribution of plasma sheath at four points around the surface of the spacecraft during reentry at the altitude of 31 km through adopting double exponential function fitting at d_1 and d_2, the other employed Gaussian function fitting at d_3 and d_4.

previous researches.[20] Also, it is expected that the maximum electron density occurs at the altitude of 31 km, as shown in Figs. 4(b) and 4(d), which is larger than those when the spacecraft is just entering or leaving the interest area. In addition, the electron density distributions of the rear of the spacecraft at each altitude are much smaller than that of the stagnation region of the spacecraft from Fig. 4, which is the reason why the transmitting antenna is always installed at this region of the vehicle in practical application.

On the other hand, the dependence of the maximum of electron density distribution around the vehicle on different distances from the spacecraft stagnation region at the altitude of 31 km is illustrated in Fig. 5(a). It is obvious that the electron density around the stagnation region is much larger than that of the aft corresponding to its severe ionization degree of the compressed shock layer in the blunt cone stagnation region. Furthermore, we investigated the detailed thickness and electron density distribution of the plasma sheath along the normal direction perpendicular to the relevant tangent direction at four distances from the spacecraft head ($d_n = 0.133$ m, 0.230 m, 0.500 m, and 1.200 m). We choose the four points at the surface of the vehicle, where two points are in the stagnation region and the other two points are away from the head region of the vehicle. As shown in Fig. 5(b), it should be pointed out that the horizontal ordinate represents the thickness of the plasma sheath encountered during spacecraft reentry at the altitude of 31 km with the maximum being up to 4.0 cm at the stagnation region. Also, we analyzed the electron density distribution profile at various d_n by exploiting two curve fitting methods. One adopted double exponential function (10) fitting at d_1 and d_2, and the other employed Gaussian function (11) fitting at d_3 and d_4, respectively. Results in Fig. 5(b) show that the electron density profile of the plasma sheath around the vehicle obeys the double exponential distribution or Gaussian distribution with correlation coefficient being up to 0.97886, 0.90434, 0.93435, and 0.91944, respectively. We could find that the electron density distributions at the aft of the vehicle are almost of the same order of magnitude (0.500 m and 1.200 m) with much smaller differences. Owing to the same coordinate ranges of four cases, an obvious fluctuation profile occurs. Near the stagnation region, we could also discover that the electron density has an evident order of magnitude change at the two cases. These results are conductive to the following researches on the transmission properties and physical mechanisms of RF and X-ray carrier through a plasma sheath

$$y = \begin{cases} y_1 + A_g e^{-(x-x_c)/t_g}, & x < x_c \\ y_2 + A_d e^{(x-x_c)/t_d}, & x \geq x_c \end{cases}, \tag{10}$$

$$y = y_0 + A e^{-\frac{(x-x_c)^2}{2w^2}}, \tag{11}$$

where y_1, y_2, A_g, A_d, t_g, t_d, and x_c are fitting parameters.

B. Transmission properties of X-ray carrier through a plasma sheath

In this section, the FDTD method was employed to investigate the X-ray transmission properties of the plasma sheath. The X-ray carrier and regular RF signal (for comparison) were mainly focused on the *Att* and T by considering different factors such as from electron density distribution and collision frequency of plasma sheath to reentry altitudes and different surface positions of spacecraft. In the present simulation, the physical properties (w_p, v_c) required were provided by referring to the computational results obtained by CFD, and the N_e satisfied the double exponential function from the above simulation results. More detailed information about X-ray interaction with plasma sheath were expected in the next discussion.

Here, we demonstrated the transmission properties of the X-ray carrier and regular RF signal through a plasma sheath encountered during spacecraft reentry. The simulation results are shown in Fig. 5, in which the relationship between the *Att* and T at different carrier frequencies ranging from RF signal (5–40 GHz) to X-ray (10^8–10^9 GHz) was identified by considering various electron peak densities and collision frequencies obtained from CFD. As illustrated in Figs. 6(a) and 6(b),

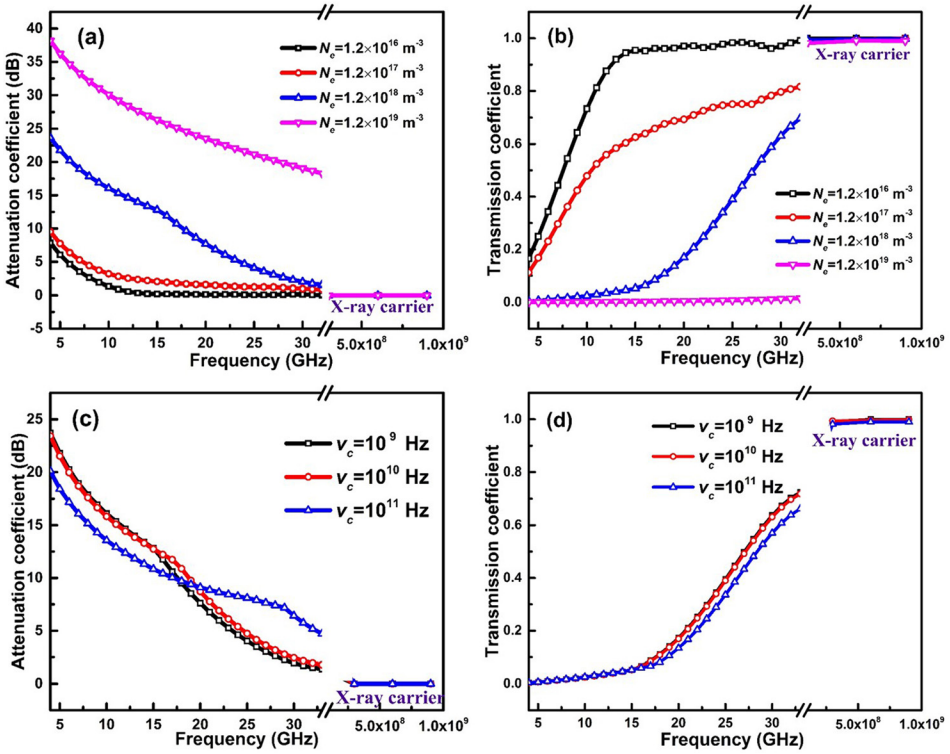

FIG. 6. Attenuation coefficient (*Att*) and Transmission (*T*) of the carrier with various frequencies ranging from the regular RF signal to X-ray at different (a) and (b) electron density distributions with the fixed collision frequency being 1 GHz, and (c) and (d) collision frequencies with the fixed electron density being $10^{19}/m^3$. All of the simulation parameters are available through the CFD simulation.

the v_c of the plasma sheath is fixed at 1 GHz, and the *Att* of RF signal decreased so sharply as the electron density increases that it hardly penetrates the plasma sheath (*T* falls to 0 with the electron density being $10^{19}/m^3$). This is supported by the fact that if RF communication were used during spacecraft reentry, the blackout communication would take place inevitably. Another important point is the apparent robustness of XCOM, the *Att* of the X-ray carrier can be totally ignored and the *T* ranges from 0.9954 to 1, even in the maximum electron density, owing to the exceedingly high carrier frequency of the X-ray. Figures 6(c) and 6(d) also illustrate that the collision frequencies of the plasma sheath do not affect the transmission properties of the X-ray, which demonstrates the potential application of XCOM through a plasma sheath encountered during spacecraft reentry compared with RF communication.

We discovered that the dependence of the electron density distribution of plasma sheath on vehicle reentry altitudes and different surface positions from the CFD simulation results is shown in Figs. 4 and 5. It is worthwhile mentioning that it relies on the spacecraft's shape, velocity, trajectory, angle of attack, and flight altitude. The *Att* and *T* of regular RF signal and X-ray carrier were also performed by considering the various reentry altitudes (25, 31, and 62 km) and distances from the spacecraft head (0.133 m–1.200 m). Simulations in Figs. 7(a) and 7(b) show that the *Att* and *T* of RF signal at various reentry altitudes have significant differences, and its propagation ceases at 31 km owing to the maximum electron density distribution here. However, this will rarely be the case for the X-ray carrier; its excellent transmission properties through a plasma sheath make it a perfect candidate medium for blackout communication and space communication. In addition, the different distances from the spacecraft head at a reentry altitude of 31 km were taken into account as well. As illustrated in Figs. 7(c) and 7(d), the closer the position of spacecraft head, the larger *Att* and the smaller *T* of RF signal, even it ceases propagation through a plasma sheath. However, the transmission properties of the X-ray carrier are not influenced by these different surface positions as well. These arguments could explain why the RF transmitting antenna is always installed at the rear of the vehicle in engineering application. Therefore, we conclude from our simulation results that X-rays as a communication carrier can transmit information through a plasma sheath, which is better than the regular RF communication.

Note that X-ray has no attenuation for transmission in space, especially when photon energy is more than 10 keV ($\lambda < 0.1$ nm) and atmospheric pressure is lower than 10^{-1} Pa.[31] However, the atmospheric environment still exists in reentry altitudes. Therefore, it is necessary to adopt a modulated X-ray source with different photon energies corresponding to the different spacecraft reentry altitudes when using X-ray uplink communication, especially during spacecraft reentry.[13]

C. Physical mechanism of X-ray carrier through a plasma sheath

To reach a deeper understanding of the physical mechanisms of XCOM carrier propagation through a plasma sheath encountered during spacecraft reentry, we have run 2D PIC simulation by using EPOCH code. According to CFD simulation results, the electron distribution of plasma sheath obeyed the double exponential model, peaking at $N_{emax} = 1.2 \times 10^{20}\ m^{-3}$. Figure 8 illustrates the variation of the E_x and the E_y of X-ray laser pulse, which could reflect its transmission properties propagating through a plasma sheath.

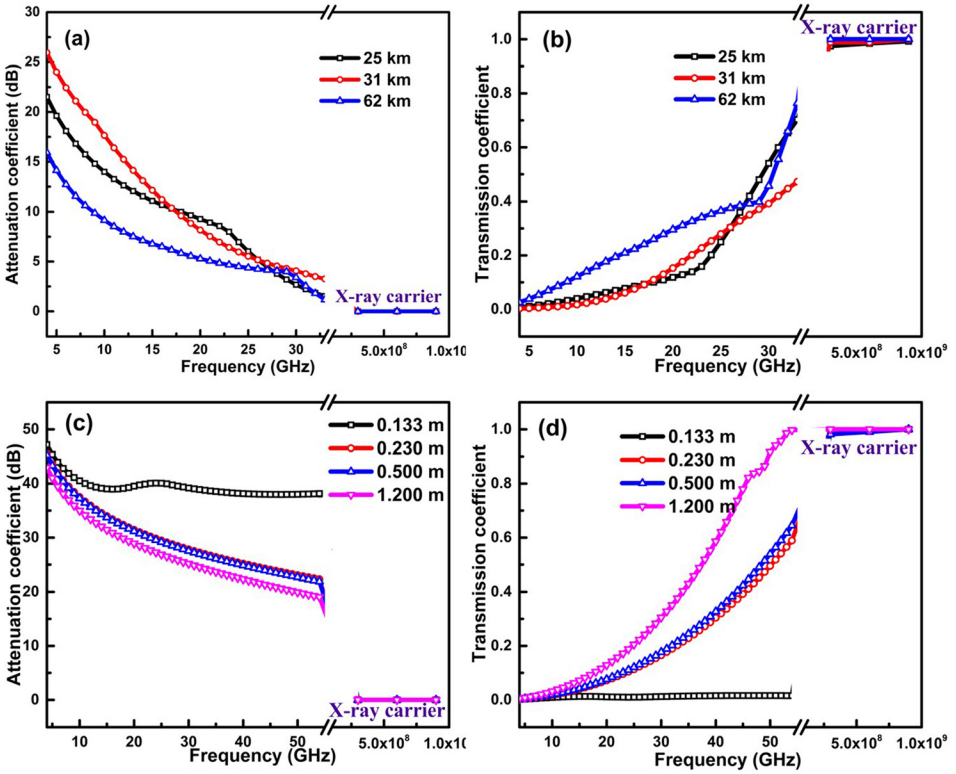

FIG. 7. Attenuation coefficient (*Att*) and Transmission (*T*) of the carrier at various frequencies ranging from the regular RF signal to X-ray at different [(a) and (b)] spacecraft reentry altitudes and [(c) and (d)] distances from the spacecraft head at a reentry altitude of 31 km obtained from the CFD simulation.

In order to evaluate the transmission properties of the X-ray carrier in plasma from the PIC perspective, we calculated transmission (T) coefficient as

$$T = \frac{Ex_{out}^2 + Ey_{out}^2}{Ex_{in}^2 + Ey_{in}^2}, \tag{12}$$

where the subscript *in* and *out* indicates the incidence and transmission of X-ray carrier through a plasma sheath, respectively. Note that the X-ray pulse phase is same in the incident boundary and transmission boundary due to the fact that the length of the simulation box along the x direction is an integral multiple of the X-ray wavelength. We extracted the E_x and E_y of the X-ray carrier propagating through a plasma sheath, as shown in Fig. 8. From Table III, we calculated the T (0.994–0.999) by using Eq. (12) which is extremely closer to 1. That is, to say, X-ray carrier has no any attenuation and also can propagate through a plasma sheath freely from a PIC perspective, which indicates a good agreement with the results obtained from FDTD simulation.

The ponderomotive force, proportional to the gradient of the X-ray laser intensity, efficiently expels plasma sheath electrons out of the regions of the X-ray laser pulse. The ponderomotive force and the relativistic increase of electron mass modify the refractive index of the plasma,[32] which generates X-ray laser pulse self-channeling in plasma and extends the propagation distance of the X-ray laser. The channel contributes to the propagation through a plasma sheath for the X-ray carrier. As illustrated in Fig. 9, the 2D PIC simulation results suggest that the physical mechanism of XCOM through a plasma sheath can be explained by the following scenario. As the X-ray pulse propagates in the plasma sheath, the relativistic and ponderomotive self-channeling effects have gradually occurred, which contribute

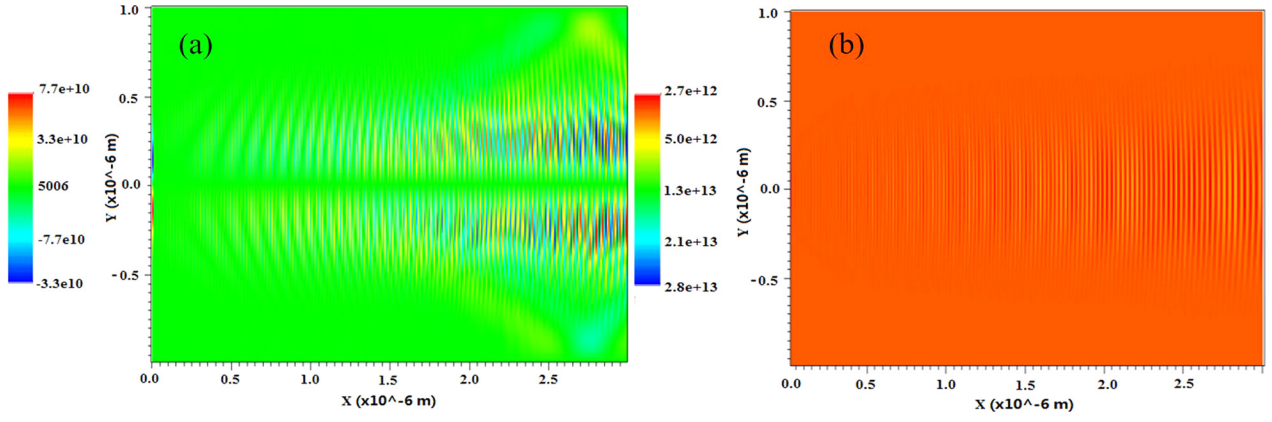

FIG. 8. 2D simulation PIC results. Snapshot of (a) the E_x (V/m) and (b) the E_y (V/m) of X-ray laser pulse propagating through a plasma sheath.

TABLE III. The E_x and E_y of X-ray laser carrier propagating through a plasma sheath.

Time (10^{-14} s)	Ex_{in} (10^{10} V/m)	Ey_{in} (10^{12} V/m)	Ex_{out} (10^{10} V/m)	Ey_{out} (10^{12} V/m)	T
1.1091	7.562	−4.265	7.55706	−4.26492	0.999
1.18832	10.34	−2.772	10.3235	−2.7716	0.997
1.26754	7.306	4.268	7.2770	4.2672	0.994
1.34677	7.724	2.687	7.7154	2.6868	0.998

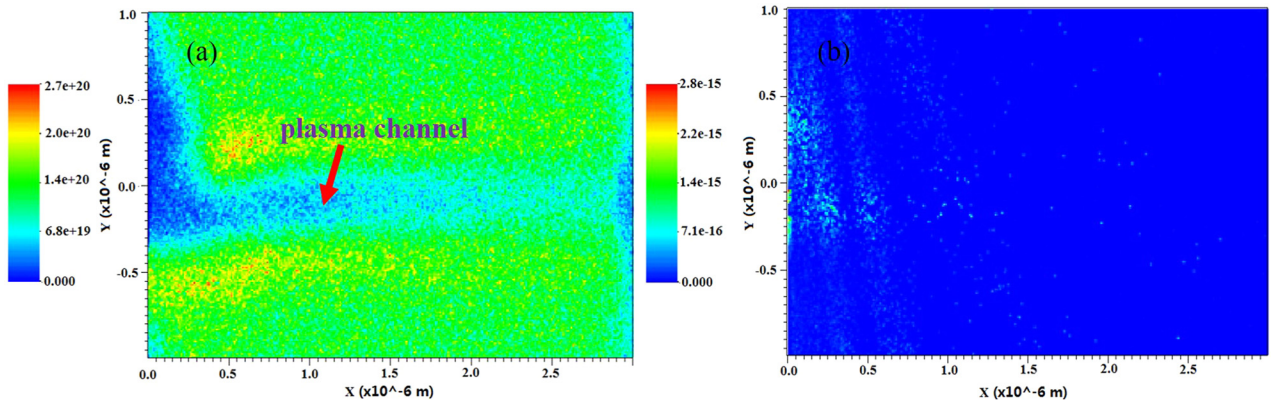

FIG. 9. 2 D simulation PIC results. Distribution of (a) the electron density (m^{-3}) in the X-Y plane, and (b) the electron energy (J) as the X-ray carrier interaction with plasma sheath.

to guiding X-ray carrier transmission. This type of plasma channels was certificated clearly from Fig. 9(a). It should be appreciated, of course, that relativistic and ponderomotive guiding are intrinsic effects for the X-ray laser pulse and will occur whenever the incident pulse power exceeds a critical threshold.[32] On the other hand, the process of X-ray laser pulse interaction with the plasma sheath should be in accord with conservation of energy, and the absorption in the X-ray carrier mainly depends on the influence of plasma electrons. The ion energy of the plasma sheath almost never changes because the mass of an ion is much larger than that of the electron. As shown in Fig. 9(b), the electron energy appears as small fluctuations initially and then remains stable all the time. That is, to say, the X-ray carrier has no obvious influence on the electron energy of the plasma sheath, which indirectly indicates that the X-ray carrier is immune to the complex vehicle reentry plasma environment as well. Generally speaking, the observation of the plasma channel effect is thus a signature that the X-ray pulse has transmitted through a plasma sheath during spacecraft reentry, which is of great importance to XCOM used in blackout communication.

IV. CONCLUSION

This paper provides an overview of the basic principles of X-ray communication (XCOM), followed by a detailed discussion of the transmission properties and physical mechanisms when X-ray carrier propagates through a plasma sheath encountered during spacecraft reentry into atmosphere. CFD simulation results offered a comprehensive electron density distribution profile around the surface of the vehicle at different reentry altitudes, peaking at $10^{14}\,cm^{-3}$. Also, we discovered that the attenuation coefficient of X-ray carriers was almost closer to 0, whereas the transmission coefficient ranged from 0.9954 to 1 by considering the various electron density distribution, collision frequency of the plasma sheath at different reentry altitudes, and surface positions through FDTD simulations. Compared with regular RF signals, the transmission properties of X-ray were not influenced by the severe reentry plasmas. In addition, the 2D PIC findings suggested that the relativistic and ponderomotive self-channeling effects occurred if the pulse power was above a critical threshold, which were beneficial to the X-ray carrier through a plasma sheath. Along with these interesting phenomena, we expect that XCOM has potential application in blackout communication during spacecraft reentry.

These results may be helpful for understanding the advantages and some related physical mechanisms of XCOM through a plasma sheath, which contribute to mitigate blackout communication encountered during spacecraft reentry into atmosphere to some extent. However, further investigations are still required to understand and better study the modulated X-ray signal source, channel transmission, and signal detection of XCOM; therefore, further studies are to be carried out in our work.

ACKNOWLEDGMENTS

This work was supported by China Postdoctoral Science Foundation (Grant No. 2016M601807), the Postgraduate Research & Practice Innovation Program of Jiangsu Province (Grant No. KYCX17_0257), and the Priority Academic Program Development of Jiangsu Higher Education Institutions (PAPD). The EPOCH code was developed under the UK EPSRC Grant Nos. EP/G054950/1, EP/G056803/1, EP/G055165/1, and EP/M022463/1.

[1]M. Kim, I. D. Boyd, and M. Keidar, J. Spacecr. Rocket **47**(1), 29 (2010).
[2]A. Mousavi, A. Esfandiari-Kalejahi, and M. Akbari-Moghanjoughi, Phys. Plasmas **23**(4), 043516 (2016).
[3]I. F. Belov, V. Y. Borovoy, V. A. Gorelov, A. Y. Kireev, A. S. Korolev, and E. A. Stepanov, J. Spacecr. Rocket **38**(2), 249 (2001).
[4]L. C. Schroeder and N. D. Akey, J. Spacecr. **10**(3), 170–174 (1973).
[5]J. Cheng, K. Jin, Y. Kou, R. Hu, and X. Zheng, J. Appl. Phys. **121**, 093301 (2017).
[6]R. A. Hartunian, G. E. Stewart, T. J. Curtiss, S. D. Fergason, and R. W. Seibold, "Implications and mitigation of radio frequency blackout during reentry of reusable launch vehicles," AIAA Paper 2007-6633, 2007.
[7]J. P. Rybak and R. J. Churchill, IEEE Trans. Aerosp. Electron. Syst. **AES-7**(5), 879 (1971).
[8]NASA Technology Roadmaps, "Communication, navigation, and orbital debris tracking and characterization systems," Report No. TA5, 2015, pp. 12–13, see https://www.nasa.gov/sites/default/files/atoms/files/2015_nasa_technology_roadmaps_ta_5_communication_and_navigation_final.pdf
[9]NASA, "Next-generation communications: 'Demonstrating the world's first x-ray communication system,'" Report No. FS-2007-10-103-GSFC (TT#7), see https://gsfctechnology.gsfc.nasa.gov/TechSheets/XRAY_Goddard_Final.pdf
[10]J. A. Bearden, Rev. Mod. Phys. **39**, 78 (1967).
[11]C. Kealhofer, S. M. Foreman, S. Gerlich, and M. A. Kasevich, Phys. Rev. B **86**, 035405 (2012).
[12]G. Porter, *See Straight Through Data Center Bandwidth Limitations with X-Rays* (CiteSeer, 2013).
[13]H. Li, X. B. Tang, S. Hang, Y. P. Liu, and D. Chen, J. Appl. Phys. **121**, 123101 (2017).
[14]N. D. Akey and A. E. Cross, Technical Report No. NASA-TN-D-5615, 1970.
[15]W. L. Jones, Jr. and A. E. Cross, Technical Report No. NASA-TN-D-6617, 1972.
[16]Fluent Inc., *Fluent 6.3 Manual 2006 Report* (Fluent Inc., New Hampshire, 2006), see http://www.hipecc.wichita.edu/pdfs/fltg.pdf.
[17]T. W. Schlatter, *Atmospheric Composition and Vertical Structure* (Earth System Research Laboratory, National Oceanic and Atmospheric Administration, NOAA Boulder, CO, USA, 2009).
[18]C. R. Wilke, J. Chem. Phys. **18**(4), 517 (1950).
[19]F. G. Blottner, M. Johnson, and M. Ellis, "Chemically reacting viscous flow program for multi-component gas mixtures," Sandia Laboratories Report No. SC-RR-70-754, Albuquerque, NM, 1971.
[20]E. Josyula and W. F. Bailey, J. Spacecr. Rockets **40**, 845 (2003).
[21]M. Ajith, L. A. Pillai, K. N. Dileep, and N. Sreenivas, Appl. Therm. Eng. **111**, 1603 (2017).
[22]J. Wilson, Phys. Fluids **9**(10), 1913 (1966).
[23]Y. Takahashi, J. Phys. D: Appl. Phys. **49**(1), 015201 (2016).
[24]M. G. Dunn and S. Kang, "Theoretical and experimental studies of reentry plasmas," NTRS, Technical Report No. NASA-CR-2232, 1973.
[25]K. G. Budden, Radio Waves in the Ionosphere (Cambridge University Press, 2009).
[26]L. Yang and Y. Xie, "LTJEC-FDTD Simulation for Electromagnetic Wave Transmission by Magnetized Plasma," Comput. Simul. **11**, 092 (2009).
[27]Y. Takahashi, K. Yamada, and T. Abe, J. Spacecr. Rocket **51**, 430–441 (2014).
[28]T. D. Arber, K. Bennett, C. S. Brady, A. Lawrence-Douglas, M. G. Ramsay, N. J. Sircombe, P. Gillies, R. G. Evans, H. Schmitz, A. R. Bell, and C. P. Ridgers, Plasma Phys. Controlled Fusion **57**, 113001 (2015).
[29]V. Horný, J. Nejdl, M. Kozlová, M. Krůs, K. Boháček, V. Petržílka, and O. Klimo, Phys. Plasmas **24**(6), 063107 (2017).
[30]X. Zhang, T. Tajima, D. Farinella, S. Youngmin, G. Mourou, J. Wheeler, P. Taborek, P. Chen, F. Dollar, and B. Shen, Phys. Rev. Accel. Beams. **19**, 101004 (2016).
[31]B. L. Henke, E. M. Gullikson, and J. C. Davis, At. Data Nucl. Data Tables **54**(2), 181 (1993).
[32]E. Esarey, C. B. Schroeder, and W. P. Leemans, Rev. Mod. Phys. **81**, 1229 (2009).